Dynamic Stall delay using High Frequency Plasma Actuation

Alexander James Lilley* and Subrata Roy†
Applied Physics Research Group, University of Florida, Gainesville, FL, 32611

Miguel R. Visbal‡
Air Force Research Laboratory, Wright-Patterson AFB, Ohio 45433, USA

The occurrence of dynamic stall vortex is delayed via plasma actuation across various pitch rates for a NACA0012 at $Re_c = 2 \times 10^5$. The phenomenon is surveyed via flow visualization of a pitching airfoil and qualitatively compared to prior implicit large-eddy simulation. The plasma actuator generates forcing that is partially normal and tangential to the leading edge. The plasma actuator's frequency tested are $St = 50.0$ and 26.6 against an unforced case. The non-dimensional pitch rates of $\Omega^+ = 0.025$, and 0.050 are considered for both actuator frequencies. The experiments are run from $\alpha = 4°$ to $\alpha = 30°$. Experimental results show an approximate delay of $3°$ while prior numerical results show a larger delay of leading edge suction collapse of approximately $7.3°$ for $\Omega^+ = 0.050$. It is speculated that the difference in dynamic stall delay is primarily due to the forcing orientation and wave type.

I. Nomenclature

c = chord length
U_∞ = freestream velocity
Re_c = chord length scaled Reynolds number $\rho U_\infty c/\mu$
St = Strouhal number based on actuation frequency, fc/U_∞
α = angle of attack
$kVpp$ = kiloVolts peak to peak
Ω = pitch rate, rad/s
Ω^+ = non-dimensional pitch rate, $\Omega c/U_\infty$

II. Introduction

Dynamic stall is characterized by a strong increase in lift beyond static stall angles followed by a rapid loss of lift due to separation of the dynamic stall vortex. In a situation with a rapidly pitching airfoil the rapid loss of lift may manifest itself as damaging vibrations. The classical example of dynamic stall vortex is the helicopter rotor blade which is long and thin causing it to be susceptible to twisting forces. The avoidance of dynamical stall is not limited to structural preservation, but also increased performance for rotorcraft and aircraft rapid maneuvering. Fundamental prior work on the physics of dynamic stall include McAlister[1], Carr[2], McCroskey[3], Visbal[4], and Ericsson and Reding[5]. Methods of suppressing dynamic stall include geometric modification of the airfoil[6][7][8], blowing mechanisms[9][10], and plasma actuators[11][12]. An obvious advantage to geometric modification of the airfoil, such as slats, flaps, and deforming leading edge, is the ability to influence the bulk flow, while disadvantage is bulk and weight of the mechanism. Blowing mechanisms while generally lighter and capable of higher frequency than geometric modification of the airfoil, provide significantly less bulk flow modification. Generally two variants of blowing mechanism are considered, mass injecting and zero-net-mass. Zero-net-mass mechanisms are generally weaker than their mass injecting counterparts, although mass injecting requires reservoirs. Plasma actuation techniques have much higher frequency response than either blowing mechanisms or geometric airfoil modification. Another canonical advantage of the plasma actuator is its light weight. Some of the disadvantages of plasma actuation include its low momentum injections and its robustness, although some work has shown that plasma actuators can function when wet.

---

[*] Research Assistant , Aerodynamic Technology Branch, AFRL/RQVA, Student Member, AIAA

[†] Professor, Mechanical and Aerospace Department, Associate Fellow, AIAA

[‡] Computational Fluid Dynamics Technical Advisor, Aerodynamic Technology Branch, AFRL/RQVA. Fellow AIAA

Table 1 Cases Considered

Non-Dimensional Pitch rate, Ω_+	Strouhal Number, St
0.025	50.0
0.025	26.6
0.025	0.0
0.050	50.0
0.050	26.6
0.050	0.0

In a numerical investigation Visbal found that high frequency, $St = 50$, forcing at the leading edge of a NACA0012 slowed the rapid onset of stall. Visbal's investigations were for $Re_c = 2 \times 10^5, 5 \times 10^5$ pitched at $\Omega^+ = 0.05$ [13]. Visbal considered two separate type of forcing 2D and 3D forcing as zero-net-mass flow at the leading edge normal to the surface. For the case at $Re_c = 2 \times 10^5$ with 2D forcing, Visbal found that the leading edge suction collapse occurred at $\alpha = 22.2°$ in comparison to the baseline case at $\alpha = 14.7°$. Visbal then concludes that high frequency pulsed control may be achieved using plasma actuators [13].

Mukherjee and Roy numerically investigated the effect of plasma actuator placement and orientation on a 2D NACA0012 at $Re_c = 1.35 \times 10^5$[12]. The non-dimensional pitch rate, Ω^+, was 0.2. They simulated dynamic stall without plasma actuation, leading edge co-flow and counter-flow plasma actuation, mid chord co-flow and counterflow actuation, trailing edge co-flow and counter-flow actuation, pulsed leading edge actuation at $St = 0.267$, and $St = 1$. The largest delay in dynamic stall found was for leading edge co-flow plasma actuation ($\alpha = 23.57$ for no actuator and $\alpha = 24.64$ for leading edge co-flow). Despite having less effect than continuous forcing, pulsed forcing, at $St = 0.267$ and $St = 1$, delayed separation from $\alpha = 23.57$ to $\alpha = 24.11$ and $\alpha = 24$, respectively[12]. Considering Mukherjee and Roy's simulation being 2D, the results showed the receptivity of leading edge forcing for a co-flow orientation delaying dynamic stall by 2.07°. Interestingly, they found that the leading edge counter flow actuation reduced the angle of dynamic stall from $\alpha = 23.57$ to $\alpha = 21.85$ reinforcing the idea of receptivity at the leading edge.

Early experimental work on suppression of dynamic stall vortex using low carrier signal frequency plasma actuators at $Re_c = 4 \times 10^6$ with a non-dimensional pitch rate, Ω^+, of 0.16 for a NACA0015 had been performed by Post and Corke[11]. For these experiments the actuator was placed at the leading edge such that the forcing was toward the suction side of the airfoil. Three variations of controller were explored: open-loop control with steady plasma actuation, open loop control with unsteady plasma actuation, and closed loop control with steady plasma actuation. The unsteady actuation is defined as an 14 kVpp 5kHz triangle wave signal with a carrier. The carrier frequencies tested were $f = 80Hz, 20Hz$ which correspond to $St = 1, 0.25$, respectively. Note that these Strouhal numbers are based on the carrier signal. The steady actuation case tested was a continuous 14 kVpp 5kHz triangle wave signal. Post and Corke found all three controlled cases improved lift over the uncontrolled cases. The open-loop control steady plasma actuation case performed better on average throughout the pitching movement than the open-loop control unsteady actuation. Although performing worse on average, the open-loop control unsteady actuation did perform better on the downward pitching movement. The closed-loop control performed best reducing the rapid lift loss and resulted in the highest integrated lift. Post and Corke found that for the best performance through full separation the optimal Strouhal number,St, was 0.25, while for delay in separation the optimal Strouhal number was unity [11].

The goal of this paper is to experimentally survey the effectiveness of plasma actuators as a high frequency approach to delaying dynamic stall. In this study both pitch rate and Strouhal number are varied. The Strouhal numbers considered are $St = 26.6$, and 50.0 for the non-dimensional pitch rates considered are $\Omega^+ = 0.025$, and 0.050. For all cases the Reynolds number is $Re_c = 2 \times 10^5$. The experimental flow visualizations are performed and qualitatively evaluated for successful delay of dynamic stall. Flow visualizations are qualitatively compared to prior work by Visbal [13].

III. Experimental Analysis - Procedure

The Applied Physics Research Group's Wind Tunnel has a $8.11 : 1$ contraction ratio, a test section cross section of $210mm \times 210mm$, and a length of $610mm$. The setup consists of a model NACA0012 airfoil with fixed disc walls. The model is pitched by a large stepper motor. The plasma actuator is embedded into the leading edge of the airfoil.The chord length of the airfoil is $100mm$, the span is $185mm$, and the freestream velocity is $30m/s$. The airfoil is pitched at

71.62 and 143.2 rpm. The actuator is run at 11 kVpp and at the frequencies of 8000 kHz and 15000 kHz. The Reynolds Number is 200,000. The airfoil is accelerated from 4° to 15° then pitched at constant rate from 15° to 30°. Beyond 30° the airfoil is decelerated. For the pitch rate of $71.62 rpm$ the angles observed were 16 through 22. For the pitch rate of $143.2 rpm$ the angles observed were 17 through 26. These angles were chosen after taking data in order to only present results of interest.

A. Model Design

The airfoil mode is designed such that between the discs there is minimal flow interference. The plates are attached via embedded bolts and fasteners. The discs are $4mm$ thick, initially $3mm$ plates were used but were shattered by the violence of the motion. The motivation for choosing to use fixed wall boundaries instead of leaving a small gap is due to investigations by Visbal and Garmann. Visbal and Garmann found that even for a 1 percent chord length gap for an aspect ratio of 4 (this experiment uses an aspect ratio of 1.85) there was significant 3D interaction [14].

The airfoil is made using a Photon Mono X masked stereolithography and 3D printed using Elegoo transparent. The body of the airfoil is sanded from 400 grit to 3000 grit to ensure the smoothest airfoil possible. To pitch the airfoil, a steel male shaft with bearing plate is fastened to the wind tunnel wall. The steel shaft plate mates to the female input integral to the airfoil structure. A shaft coupler mates the male stepper motor to the steel shaft plate. The coupler is made from Siraya Blu, a strong engineering grade UV resin.

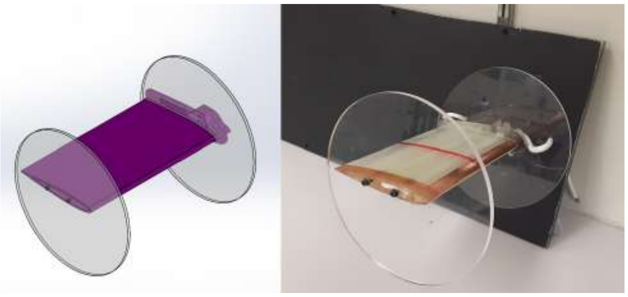

Fig. 1 Isometric view of the airfoil model used. Two transparent discs are used to implement the fixed wall condition

The actuator is a standard linear actuator contoured around a NACA0012 leading edge. The exposed electrode is $25mm$ beginning at the leading edge. The embedded electrode is $3.125mm$ held via insert in the leading edge (Fig 2). The positioning is such that the forcing begins at the leading edge.

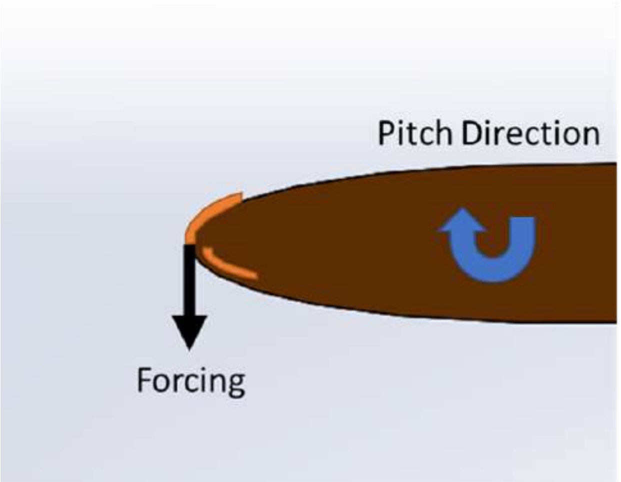

Fig. 2 Forcing and actuator placement. In orange the electrodes are depicted. The upper orange is the exposed electrode and the lower is the embedded electrode

The actuator is powered using a signal generator, audio amplifier and custom transformer. The signal is generated via a Tektronix arbitrary function generator (Model AFG3022B). The signal is passed to a QSC 1850 HD RMX audio amplifier and then through custom-made Corona Magnetic transformer (1:245 ratio).The output of the custom amplifier is measured via Tektronix DPO2014. The output is connected to the exposed electrode. For all cases the output signal is sinusoidal and the magnitude is 11.0 kVpp. A schematic can be seen in Fig. 3.

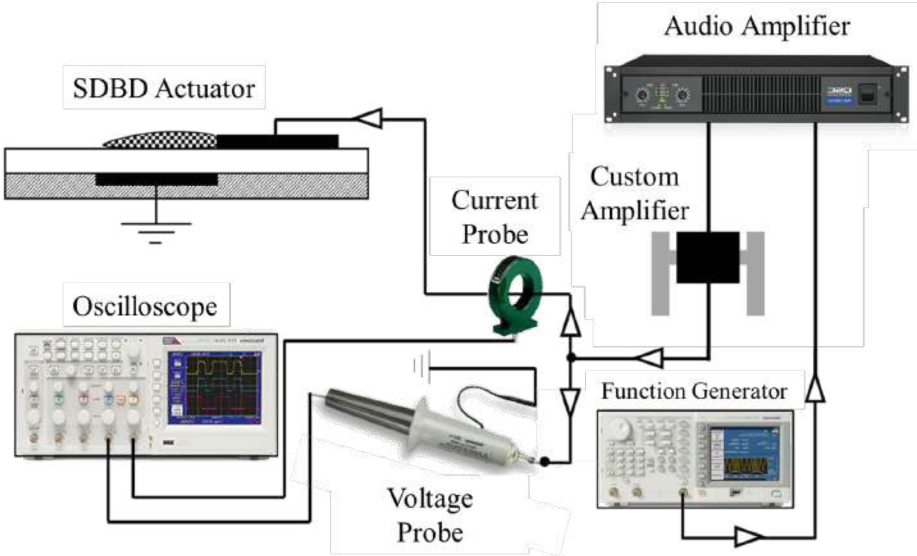

Fig. 3 Electronic setup for powering the plasma actuator

B. Flow Visualization

The seed is introduced at the entrance of the tunnel such that only a thin plane is seeded. The seed is generated using a 400 Watt thermal fogging machine. The mixture used is a 3:2 distilled water to glycerine mixture. To illuminate the seed, a single laser pulse from a $523nm$ New Wave Research 14 Hz Nd:YAG is used.

Two 2048 × 2048 CCD Imager Pro X Cameras are used to record the flow visualization. Camera 1 lies directly parallel to the airfoil. Using a 45 degree mirror Camera 2 takes lies slightly off parallel from the airfoil edge. The purpose of Camera 1's positioning is to observe the leading edge and the purpose of Camera 2's positioning is to observe the entire airfoil. Both cameras are triggered at the same time and have the same exposure time of $5\mu s$.

To avoid laser reflections, for purposes of preserving cameras and observing near wall effects Rhodamine 6G paint is used in conjunction with optical camera filters. The Rhodamine 6G paint fluoresces $532nm$ primarily in the $590nm$ range. Using a $532 \pm 2nm$ narrowband pass optical filter, most of the fluoresced light at the surface is filtered out. One of the common methods of applying Rhodamine 6G to a surface is to dope acrylic paint with ethanol and mix Rhodamine 6G. We found that clear acrylic nail polish mixed with Rhodamine 6G provided a suitable replacement. The airfoil is painted only along the illuminated plane.

C. Mechanical Design and Synchronization

One of the main challenges with the pitching airfoil experiment is producing reliable consistent results. A closed loop stepper motor was chosen to pitch the airfoil due to its accurate movement. Stepper motors function by an array of magnets which hold the motor shaft at a specific angle, when pulsed the motor performs a step. Closed loop stepper motors track their steps using encoders such that missed steps are corrected for. Due to the large amount of rotational inertia, it is necessary that the airfoil is accelerated from 0° to 15° angle of attack and maintained at constant pitch rate until 30°. The velocity profile is seen in Fig. 4.

Pulsed lasers function by continuously charging and discharging, this is called the Q-switch. The trigger which allows the laser to discharge via light emission at the next charge peak is called the firelamp. The Imager Pro X cameras are synchronized to the laser via PTU-9 from LaVision. The PTU-9 is a timing unit provides a Q-switch output to the laser and a trigger for the camera. The system functions as follows: the Arduino Due waits for the user to press the

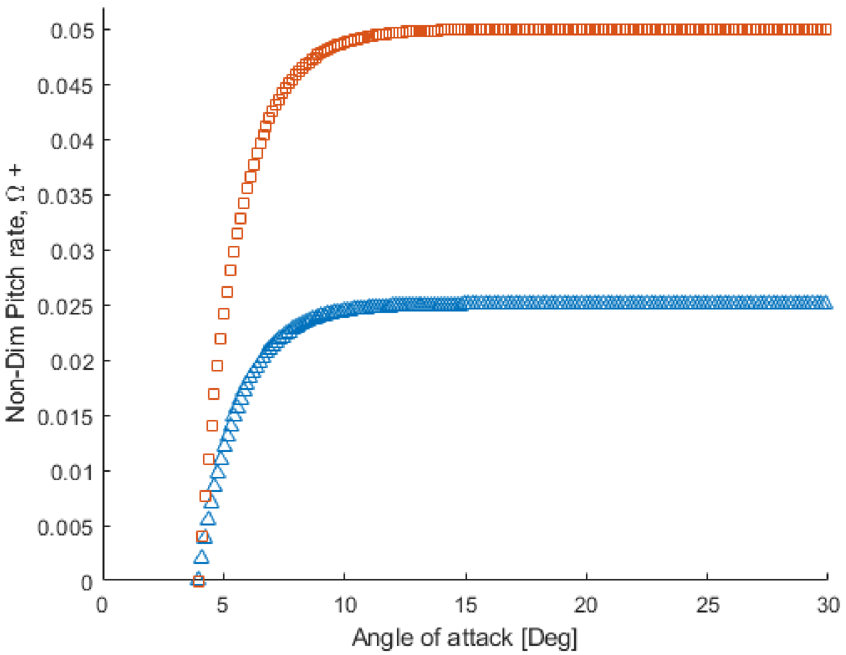

Fig. 4 The two pitch rates considered in the experiments. The squares represent the $\Omega^+ = 0.050$ **and the triangle represents** $\Omega^+ = 0.025$

start button. Once the start button is pressed, the Arduino Due will wait for a Q-switch peak charge. The Arduino Due will then send a signal to the PTU-9 such that the next peak charge of the Q-switch the laser will fire along with both cameras. Before the firing of the laser, the Arduino Due sends command to pitch the airfoil. Because the time until the discharge is known and so is the pitch rate, the angle can be modulated by changing the timing of pitching the airfoil. Fig. 5 shows a schematic of the system.

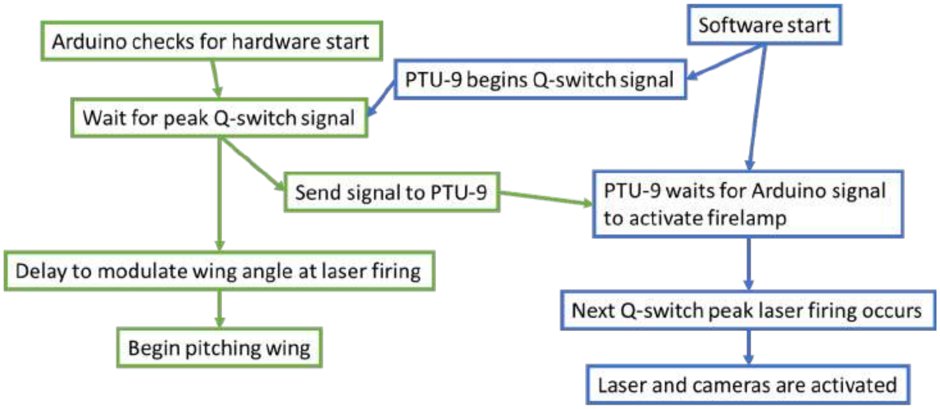

Fig. 5 Synchronization of the pulsed laser, camera, and pitching airfoil

The two timing components for this system, the PTU-9 and Arduino Due could be modified for a single system. The reason a single system is not used if for convenience and safety. The PTU-9, Imager Pro X Cameras, and New Wave Research laser are part of a single package. The system is inherently safer because it requires a software start, followed by a hardware start (depress a button to begin the sequence). The time resolution of the PTU-9 is 10 ns, while the Arduino Due is less than 62.5 ns. Both time scales are significantly smaller than physical phenomena observed.

IV. Results and Discussion

The data is organized such that the columns correspond to the angle of the airfoil and the rows correspond to the Strouhal number, St. The Strouhal number is determined by the frequency of actuation. There are two types of experimental data shown in this paper, near leading edge visualizations and full airfoil visualizations. The flow visualizations seen in Fig. 7 are from Camera 1 that is observing only the leading edge of the airfoil, while figures seen in Fig. 6 are from Camera 2 which observes the entire airfoil. This process is the same for both the $\boldsymbol{\Omega} = 0.025$ and $\boldsymbol{\Omega} = 0.050$ case.

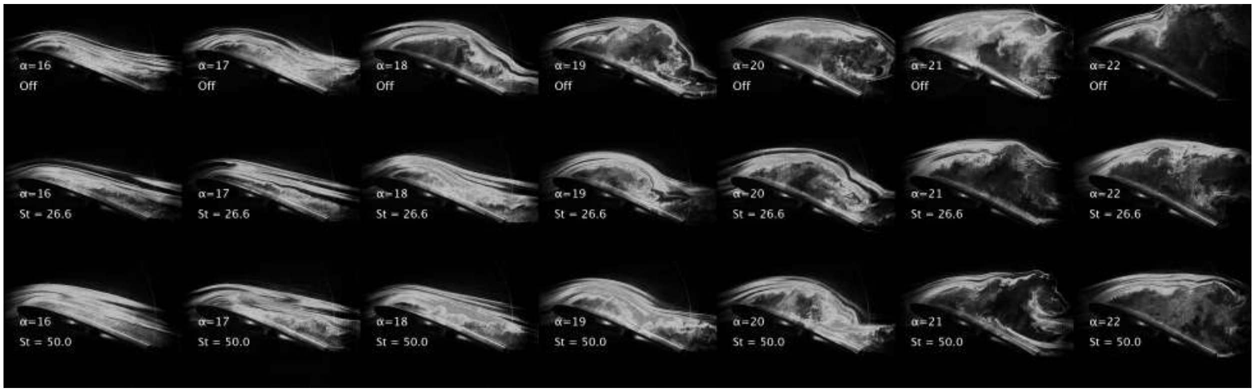

Fig. 6 Flow visualization from Camera 2 for a non-dimensionalized pitch rate of $\Omega^+ = 0.025$. This is an image of the entire airfoil

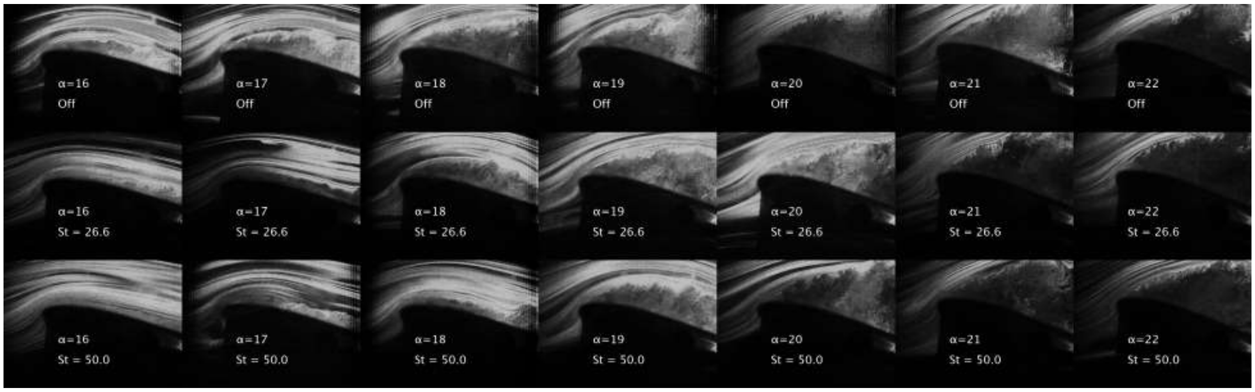

Fig. 7 Leading edge flow visualization from Camera 1 for a non-dimensionalized pitch rate of $\Omega^+ = 0.025$. This is an image near the leading edge

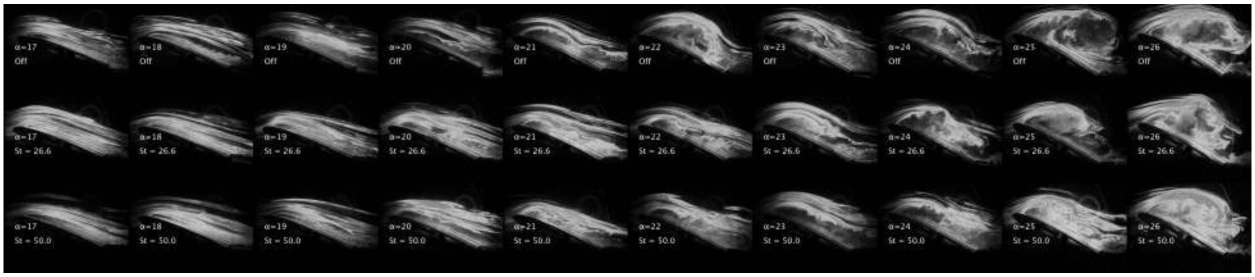

Fig. 8 Flow visualization from Camera 2 for a non-dimensionalized pitch rate of $\Omega^+ = 0.050$. This is an image of the entire airfoil

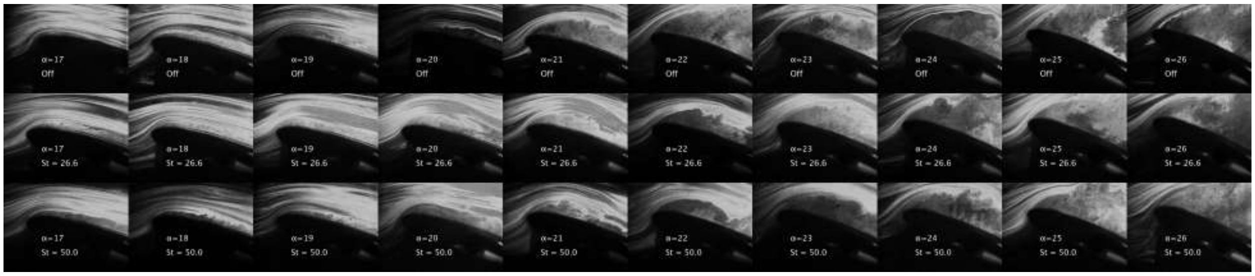

Fig. 9 Leading edge flow visualization from Camera 1 for a non-dimensionalized pitch rate of $\Omega^+ = 0.050$. This is an image near the leading edge

A. Experiments - Ω=0.025

As seen in Figs 10,6 at $\alpha = 18°$, there is a more coherent separation bubble for the actuator off case than all other cases. When observing the leading edge images we note that for $\alpha = 18°$ the actuator off case displays the largest amount of separation but all cases appear completely separated for angle of attack greater than $\alpha = 19°$ (Fig. 11,7). Images of the full airfoil show a dynamic stall vortex at $\alpha = 19°$ for actuator off and a more suppressed dynamic stall vortex at $\alpha = 20$ for actuator on $St = 26.6, 50.0$ (Fig 6). It is difficult to make a confident conclusion between the effectiveness of the St=26.6 and St=50.0 cases, but it appears St=50.0 is marginally more effective in comparing $\alpha = 18°, 19°$ (Fig. 10,11). When considering the difference in effectiveness between St=26.6 and St=50.0 cases, the St=50.0 case appears less separated in $\alpha = 18°$ for both leading edge and full airfoil view (Figs. 7,6). This suggests that the St=50.0 is more effective in delaying dynamic stall than St=26.6.

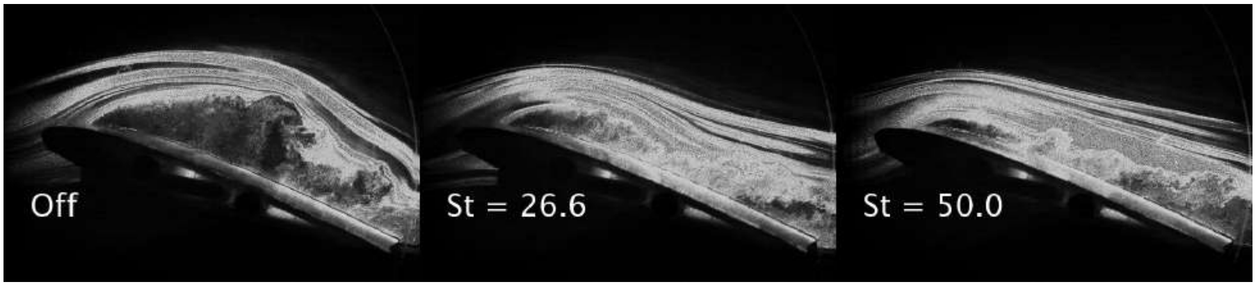

Fig. 10 Full chord length flow visualization from Camera 2 for a non-dimensionalized pitch rate of $\Omega^+ = 0.025$ at angle of attack of $18°$. Note the significant difference in separation

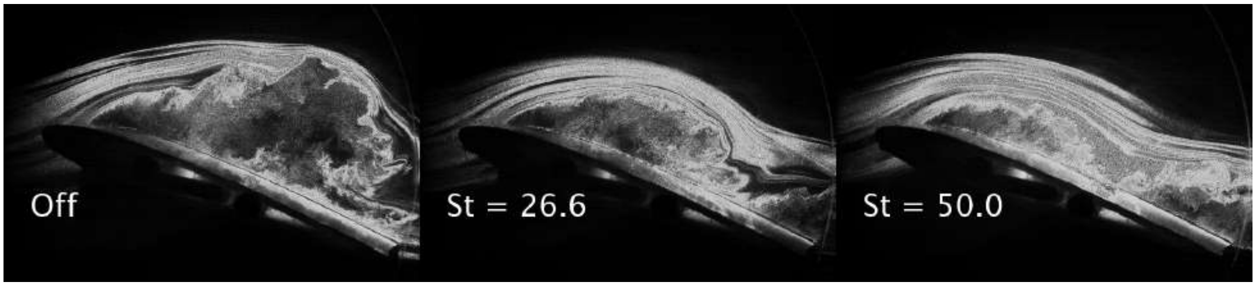

Fig. 11 Full chord length flow visualization from Camera 2 for a non-dimensionalized pitch rate of $\Omega^+ = 0.025$ at angle of attack of $19°$. Note the significant difference in separation

B. Ω=0.050

Dynamic stall is characterize by the turbulent boundary layer that creeps from the trailing edge to leading edge as angle of attack increases until $\alpha = 20°$ (As seen experimentally and numerically see Fig. 8). Leading up to dynamic stall an extreme increase in fluctuations can be seen in Fig. 8 at approximately $\alpha = 19°, 20°$, also seen by Visbal[13]. The fluctuations are more visible when they convect and grow downstream as the non-homogeneous turbulence separating the homogeneous turbulence and laminar flow (See Fig. 8 at $\alpha = 19°$). The separation of the dynamic stall vortex from the suction side leading edge is precipitated by high pressure fluid moving upstream toward the leading edge. When the high pressure encounters the low pressure dynamic stall vortex, the vortex separates causing suction collapse near the leading edge [13]. At $\alpha = 21°$ the dynamic stall vortex can clearly be seen Fig. 16. Once the dynamic stall vortex is formed it slowly convects down the chord length moving farther from the airfoil surface.

For the $\mathbf{\Omega} = 0.050$ case, figs 8,9, the results were similar to the $\mathbf{\Omega} = 0.025$ case in forcing effectiveness. Due to the difference in pitch rate, for $\mathbf{\Omega} = 0.050$ half the time passes per degree compared to the $\mathbf{\Omega} = 0.025$ case. Therefore it is expected that $\mathbf{\Omega} = 0.050$ will form a dynamic stall vortex at a larger angle of attack. Qualitatively, the dynamic stall vortex appears at $\alpha = 22°$ for the actuator off case, while similar formation appears at $\alpha = 24, 25$ for St=26.6 and $\alpha = 25°$ for St=50.0 (Fig. 8). Near leading edge images show similar results with small amounts of separation at $\alpha = 22$ for St=26.6 and St=50, while actuator off shows large amounts of separation at $\alpha = 22°$ (Figs. 13,14). Large near leading edge separation comparable to actuator off $\alpha = 22°$ occurs at $\alpha = 24°, 25°$ for St=26.6 and $\alpha = 25$ for St=50.0 (see Figs 13,14,15). Between the St=26.6 and St=50.0 case, actuation at St=50.0 appears more effective in delaying dynamic stall vortex. There is marginally more separation for the full airfoil images at $\alpha = 22°, 24°$ for St=26.6 than St=50.0 (Fig.13,15). When considering the the near edge images there is less separation for St=50.0 for all images until $\alpha = 25°$ where distinguishing differences in separation is more difficult. Similar to the $\mathbf{\Omega} = 0.025$ cases, $\mathbf{\Omega} = 0.050$ case results suggests that the St=50.0 is more effective in delaying dynamic stall than St=26.6.

For the actuator on case the dynamic stall vortex is not apparent at $\alpha = 21$. Instead an attached turbulent boundary layer is seen when comparing these experimental results to the numerical results of Visbal [13] (Fig. 17). It qualitatively appears that the for angles of attack greater than $\alpha = 21°$, the experimental turbulent boundary layer is larger and leads to a dynamic vortex like situation for $\alpha = 25°, 26°$, while numerical simulation shows a thickening of the turbulent boundary layer with no coherent dynamic stall vortex. This leads to a need to be able to establish, even if qualitative, the performance of the experiment. The images for St = 50.0 at all α were rotated and super imposed on $\alpha = 21°$, actuator off. The absolute difference in the image was taken, where darker represents more difference and lighter represents more similarity (Fig 12). From Fig. 12 the flow is visually similar for $\alpha = 21°$, actuator off and $\alpha = 24°$, St=50.0 indicating at least a delay of $\alpha = 3°$ occurs. In Fig. 12 for $= 19°$, actuator off and $\alpha = 24°$, St=50.0 (the rightmost image), the majority of image difference is in the free stream laminar streaks except near the fluctuations on the border of the separation formation. Note that the experimental St=50.0 case does eventually lead to a coherent dynamics stall vortex, while a similar numerical case by Visbal does not [13] (Fig. 8).

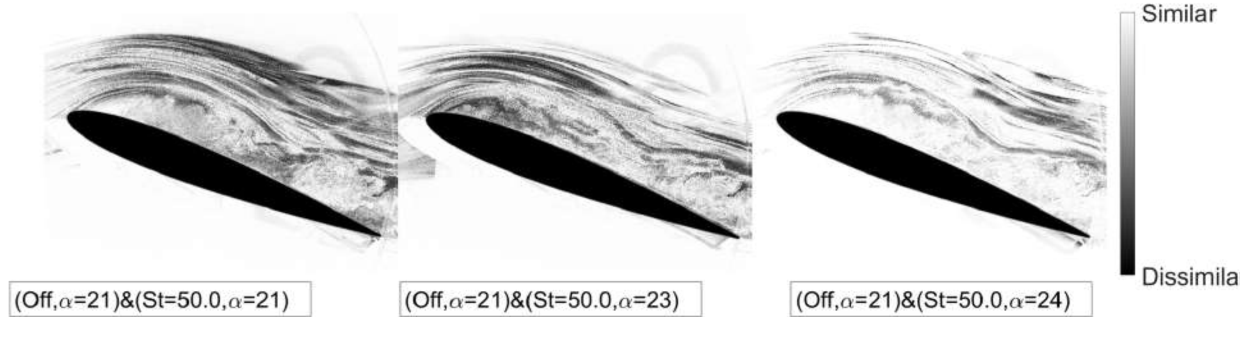
(Off,α=21)&(St=50.0,α=21)
(Off,α=21)&(St=50.0,α=23)
(Off,α=21)&(St=50.0,α=24)

Fig. 12 Image difference of various α at St=50.0 compared to $\alpha = 21°$ at actuator off for $\Omega^+ = 0.050$. Here darker colors indicate difference and lighter colors indicate more similarity. Note how similar $\alpha = 21°$ at actuator off is to $\alpha = 24°$ at St=50.0, indicating a delay of $3°$

As stated before there are similarities between the numerical work by Visbal[13] and the experiments shown in this paper. As seen in Fig 16, the leading edge vortex is apparent as well as the trailing edge vortex. The difference in the vortex size and shape may be due to factors later. Another possibility is that the flow visualization is not an accurate representation of the vorticity magnitude. From Fig. 17, the turbulent detached layer appears marginally larger for the experimental case than Visbal's numerical case[13]. It appears that the fluctuations are what is causing the larger detached turbulent layer. There are a multitude of considerations necessary when evaluating the difference between the experiments at St=50.0 presented here and the work of Visbal [13]. The major differences include: forcing, aspect ratio, and surface of the wing. Visbal found that fluctuation spectrum near the leading edge at $Re_c = 5 \times 10^5$ and $\alpha = 8$ for a static case has a peak at Strouhal$\approx$ 120 [13]. his prompted the simulation of a leading edge forced case at St=50.0. It is suspect better performance in Visbal's simulation may be due the square wave pulsed zero net max flux force versus the forcing of the actuator. Due to the nature of the square wave, the superharmonics are forced as well, while for the actuator the superharmonics are forced to a lesser degree. Prior work[15][16] has shown from current discharge that the actual force exerted on the fluid is intermittent. This difference in forcing of the superharmonics is supported by the fact that experimental case at St=26.6 did not perform as well as St=50.0. The forcing performed by Visbal [13] is also normal to the surface whereas it is suspected most of the plasma actuator forcing is tangential to the surface. The ramifications of this may lead to lesser mixing of low speed neart wall fluid and highspeed freestream. The aspect ratio also plays a significant role in the flow . More recent work by Visbal and Garmann shows that for an aspect ratio of 2.0 at $Re_c = 2 \times 10^5$ fixed wall conditions, the flow is similar to periodic conditions during the uptstroke [14]. The aspect ratio for the experiment is 1.85 with fixed walls conditions, while Visbal's simulations used periodic conditions with a span of $0.1c$ [13]. Finally the surface contour of the wing plays a role. Although the NACA0012 model is smooth up to 3000 grit, the exposed electrode of the actuator has a thickness of $70\mu m$ which may trip the flow to some amount. The results of this paper indicate that were quantitative comparison between numerical and experimental results performed, the future work must have an agreement in forcing and boundaries to ensure a justified comparison.

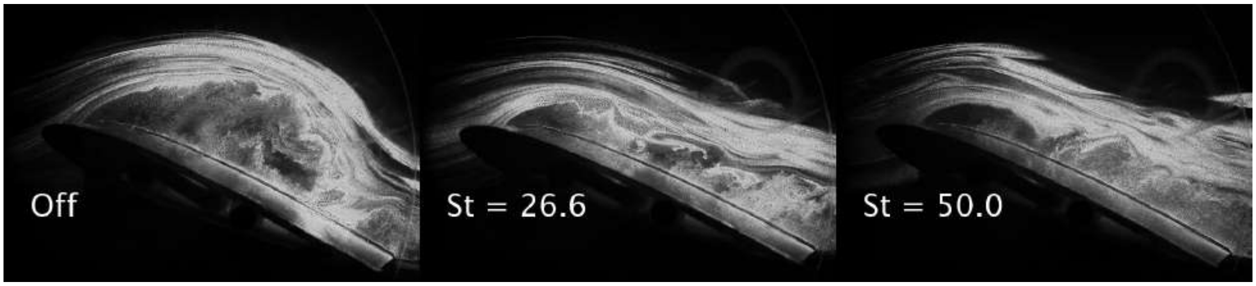

Fig. 13 Full chord length flow visualization from Camera 2 for a non-dimensionalized pitch rate of $\Omega^+ = 0.050$ at angle of attack of $22°$.

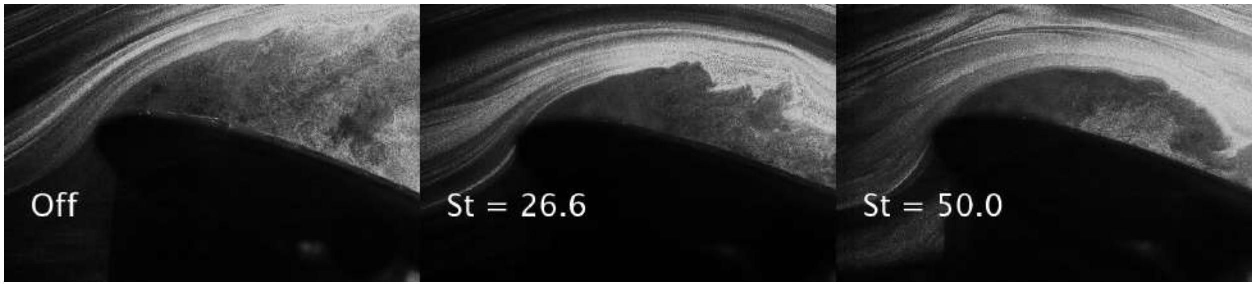

Fig. 14 Leading edge flow visualization from Camera 1 for a non-dimensionalized pitch rate of $\Omega^+ = 0.050$ at angle of attack of $22°$.

V. Conclusion

The effectiveness of plasma actuator Strouhal number on delaying dynamic stall was observed via flow visualization for non-dimensional pitch rate $\Omega^+ = 0.025, 0.050$. From the experimental results it was qualitatively that determined St=50.0 was more effective in delaying dynamic stall than St=26.6 for both $\Omega^+ = 0.025, 0.050$. The St=50.0 experimental case was compared to similar work [13] and found qualitative agreement in dynamic stall vortex location. Although it may be crude to compare leading edge suction collapse to image difference, it is estimated that the experimental delay in stall is approximately 3° while numerically suction collapse was delayed by approximately 7.3° angle of attack [13] for pitch rate of $\Omega^+ = 0.050$. It is suspected the difference is due to the simulated surface normal square forcing interacting with superharmonics more effectively than sinusoidal forcing by plasma actuator. More investigations and optimizations

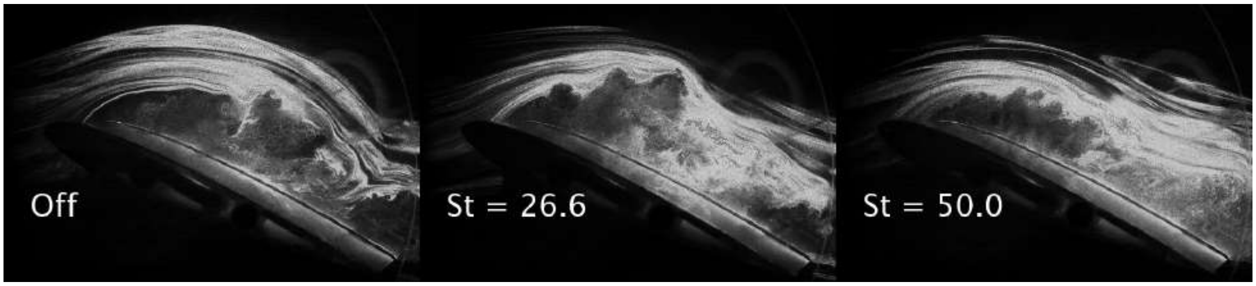

Fig. 15 Full chord length flow visualization from Camera 2 for a non-dimensionalized pitch rate of $\Omega^{+} = 0.050$ at angle of attack of $24°$.

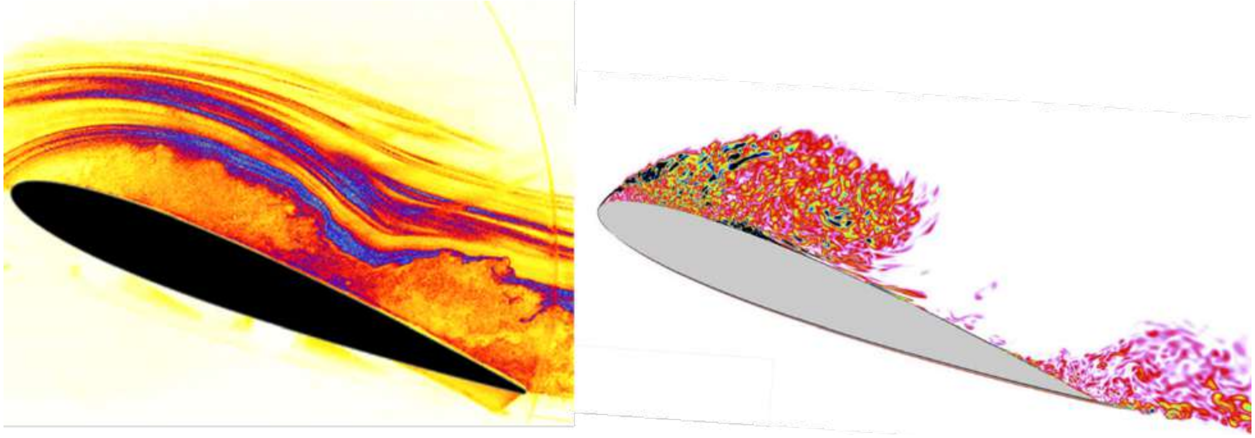

Fig. 16 Actuator off case at $\alpha = 21$. On the left an experimental flow visualization. On the right contours of the vorticity magnitude from numerical simulation at $\alpha = 20.9$ by Visbal [13]

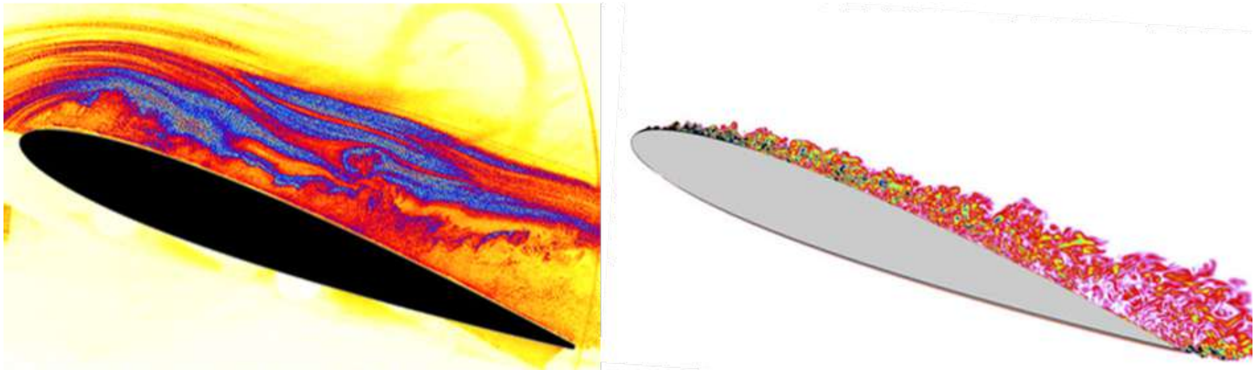

Fig. 17 Actuator on, Strouhal = 50.0 case at $\alpha = 21$. On the left an experimental flow visualization. On the right contours of the vorticity magnitude from numerical simulation at $\alpha = 20.9$ by Visbal [13] with zero net mass leading edge forcing at Strouhal = 50.0

will be performed to the actuator forcing, actuator geometry and/or arrangement, including the exploration of other Strouhal numbers. In order to compare numerical work to experimental future experiments will include Particle Image Velocimetry, therefore direct flow comparisons can be made.

Acknowledgments

This work was partially supported by the AFRL funding through OAI-C2644-19296. The first author would like to thank the APRG members who helped build the wind tunnel. The first author would like to thank to the Graduate Student Preeminence Award (GSPA) at the University of Florida and the Student Stem Employment Program (SSEP) under the United States Air Force for funding support.

References

[1] McAlister, K., Carr, L., and W, M., "Dynamic stall experiments on the NACA0012 airfoil," *TP1100*, 1978.

[2] Carr, L., McAlister, K., and McCroskey, W., "Analysis of the development of dynamic stall based on oscillating airfoil experiments." *TN D-8382*, 1977.

[3] McCroskey, W., "The phenomenon of dynamic stall," *TM 81264*, 1981.

[4] Visbal, M. R., "On Some Physical Aspects of Airfoil Dynamic Stall," *Proceedings of the International Symposium on Non-Unsteady Fluid Dynamics*, Vol. 92, 1990.

[5] Ericsson, L., and Reding, J., "Fluid dynamics of unsteady separated flow. Part II. Lifting surfaces," *Progress in Aerospace Sciences*, Vol. 24, No. 4, 1987, pp. 249–356. https://doi.org/10.1016/0376-0421(87)90001-7.

[6] Carr, L., and McAlister, K., *The effect of a leading-edge slat on the dynamic stall of an oscillating airfoil*, 1983. https://doi.org/10.2514/6.1983-2533.

[7] Chandrasekhara, M., Wilder, M., and Carr, L., "Unsteady Stall Control Using Dynamically Deforming Airfoils," *AIAA Journal*, Vol. 36, No. 10, 1998, pp. 1792–1800.

[8] Heine, B., Mulleners, K., Joubert, G., and Raffel, M., "Dynamic Stall Control by Passive Disturbance Generators," *AIAA Journal*, Vol. 51, No. 9, 2013.

[9] Greenblatt, D., and Wygnanski, I., "Dynamic Stall Control by Periodic Excitation, Part 1: NACA 0015 Parametric Study," *JOURNAL OF AIRCRAFT*, Vol. 38, No. 3, 2001.

[10] Müller-Vahl, H. F., Nayeri, C. N., Paschereit, C. O., and Greenblatt, D., "Dynamic stall control via adaptive blowing," *Renewable Energy*, Vol. 97, 2016, pp. 47–64.

[11] Post, M. L., and Corke, T. C., "Separation Control Using Plasma Actuators: Dynamic Stall Vortex Control on Oscillating Airfoil," *AIAA Journal*, Vol. 44, No. 12, 2006, pp. 3125–3135. https://doi.org/10.2514/1.22716.

[12] Mukherjee, S., and Roy, S., "Enhancement of lift and drag characteristics of an oscillating airfoil in deep dynamic stall using plasma actuation," *50th AIAA Aerospace Sciences Meeting including the New Horizons Forum and Aerospace Exposition*, , No. 2012-702, 2012. https://doi.org/10.2514/6.2012-702.

[13] Visbal, M. R., "Numerical Exploration of Flow Control for Delay of Dynamic Stall on a Pitching Airfoil," *32nd AIAA Applied Aerodynamics Conference*, 2014. https://doi.org/10.2514/6.2014-2044.

[14] Visbal, M., and Garmann, D., "Investigation of Spanwise End Effects on Dynamic Stall of a Pitching Wing Section," *Journal of Aircraft*, Vol. 56, 2019, pp. 1–13. https://doi.org/10.2514/1.C035427.

[15] Tang, A., Vaddi, R. S., Mamishev, A., and Novosselov, I. V., "Empirical Relations for Discharge Current and Momentum Injection in DBD Plasma Actuator," *J. Apple. Phys. D.*, Vol. 10, 2021, pp. 1361–6463.

[16] Boeuf, J. P., Lagmich, Y., and Pitchford, L. C., "Contribution of positive and negative ions to the electrohydrodynamic force in a dielectric barrier discharge plasma actuator operating in air," *J. Apple. Phys.*, Vol. 106, 2009, p. 023115.